X-ray energy spectrum estimation based on a virtual computed tomography system

Takayuki Higuchi and Akihiro Haga

Department of Biomedical Sciences, Tokushima University, Tokushima 770-8503, Japan

E-mail: haga@tokushima-u.ac.jp

Abstract. This paper presents a method for estimating the X-ray energy spectrum for computed tomography (CT) in the diagnostic energy range from the reconstructed CT image itself. To this end, a virtual CT system was developed, and datasets, including CT images for the Gammex phantom labeled by the corresponding energy spectra, were generated. Using these datasets, an artificial neural network (ANN) model was trained to reproduce the energy spectrum from the CT values in the Gammex inserts. In the actual application, an aluminum-based bow-tie filter was used in the virtual CT system, and an ANN model with a bow-tie filter was also developed. Both ANN models without/with a bow-tie filter can estimate the X-ray spectrum within the agreement, which is defined as one minus the absolute error, of more than 80% on average. The agreement increases as the tube voltage increases. The estimation was occasionally inaccurate when the amount of noise on the CT image was considerable. Image quality with a signal-to-noise ratio of more than 10 for the basis material of the Gammex phantom was required to predict the spectrum accurately. Based on the experimental data acquired from Activion16 (Canon Medical System, Japan), the ANN model with a bow-tie filter produced a reasonable energy spectrum by simultaneous optimization of the shape of the bow-tie filter. The present method requires a CT image for the Gammex phantom only, and no special setup, thus it is expected to be readily applied in clinical applications, such as beam hardening reduction, CT dose management, and material decomposition, all of which require exact information on the X-ray energy spectrum.

1. Introduction

To develop a technique using computed tomography (CT) imaging, such as material decomposition, physical density/stopping power ratio estimations, and artifact corrections, it is important to consider an X-ray energy spectrum. Owing to their high photon flux, methods for indirectly evaluating the incident X-ray spectrum in CT devices have been investigated. For instance, employing a Compton spectrometer (Matscheko and Carlsson 1989; Maeda, Matsumoto, and Taniguchi 2005; Duisterwinkel et al. 2015), where the photon flux is suppressed at the detector owing to the measurement of the scattered X-rays. However, the preparation of the device is costly, and careful calibration is required to avoid the influence of absorption in the scatter medium and dependence on

the detector efficiency. Therefore, it is difficult to apply this method to popular clinical devices. An alternative approach is Monte Carlo (MC) simulation, which includes all physical processes at the required accuracy level (Taleei and Shahriari 2009; Bazalova and Verhaegen 2007; Spezi et al. 2009; Hioki et al. 2014). For the MC simulation of a CT system, detailed information about the head structure of the scanner, as well as its material components, is required because it has a large influence on the energy distribution. However, this information is not available for commercial devices because of proprietary rights. In particular, a bow-tie filter can be used to make the radiation signal uniform within the dynamic range of the detector, and to reduce unnecessary radiation dose to the peripheries of a patient, which remains proprietary to most CT vendors. Because the X-ray spectrum is altered with its inherent direction depending on the thickness of the bow-tie filter, knowledge of the exact profiles from different bow-tie filters is crucial to model the imaging process of modern helical CT scanners.

Spectrum estimation of the incident X-ray has been performed with various approaches for formulating the X-ray transmission as a linear system on a specific phantom of known material and thickness (Silberstein 1932; Ruth and Joseph 1997; Perkhounkov et al. 2016; Zhao, Xing, et al. 2017; Sidky et al. 2005; Duan et al. 2011; Ha et al. 2019; Francois, Catala, and Scouarnec 1993; Stampanoni et al. 2001; Waggener et al. 1999; Armbruster, Hamilton, and Kuehl 2004; Leinweber, Maier, and Kachelrieß 2017). Despite these efforts, most studies have either not involved the bow-tie filter or only considered the influence of the presence of a specific bow-tie filter (Zhao, Vernekohl, et al. 2018; Lin et al. 2014). The bow-tie filter alters the spectrum shape from that at the X-ray source, and the transformation should be evaluated by considering the bow-tie filter thickness in each X-ray direction. However, the composing material, as well as the shape of the bow-tie filter, is not available in most CT vendors. Therefore, the bow-tie profile should be estimated simultaneously with the X-ray spectrum, where the transmission profile has been determined from the measured data while knowing the X-ray source-to-isocenter distance and chamber-to-isocenter distance (Boone 2010; Whiting et al. 2014; McKenney et al. 2011). In particular, Yang *et al* developed an equivalent aluminum thickness profile of a bow-tie filter, and the incident X-ray energy spectrum in a CT scanner with simultaneous geometrical calibration (Yang et al. 2017). This method provides an accurate estimation by using the information of the half-value layer (HVL) at the central X-ray beam, where the thickness of the bow-tie filter is a minimum. However, a specific measurement utilizing two fiducial markers to determine the related geometrical parameters in the CT scanner is required.

In the present study, we developed a method to estimate the energy spectrum from the reconstructed CT image without geometrical calibration, even in the presence of a bow-tie filter. We proposed a machine-learning approach to estimate the X-ray energy spectrum of clinical CT systems with and without the bow-tie filter using the Gammex phantom (Gammex Inc., Middleton, WI) as a commonplace phantom. To this end, we generated various CT images labeled by the corresponding X-ray spectrum using a virtual CT system, which first generated various X-ray spectra, and then simulated the

projections (or sinograms) from the information of elemental composites in the Gammex phantom for each spectrum. Subsequently, CT reconstruction was performed. By training a machine learning model with the CT-spectrum dataset, the X-ray spectrum in an arbitrary CT device can be efficiently estimated by acquiring only the CT image of the Gammex phantom in that device. An adaptation of a generative model to generate the training dataset has received considerable attention (Bishop and Nasrabadi 2006; Hastie et al. 2009). In addition, an artificial neural network (ANN) model combined with a generative model was recently proposed for spectrum estimation (Hasegawa et al. 2021), where the percent depth doses with various X-ray spectra were generated by the spektra toolkit (Punnoose et al. 2016); an ANN model to estimate the spectrum was developed with the PDD data as an input. This approach is essentially different from the other approaches proposed from the viewpoint of artificially generated datasets; the training X-ray spectra and the corresponding PDDs are *generated* based on the generative model. However, this method has only been applied in cone-beam CT geometry. To the best of our knowledge, no study has used the generative helical CT model in energy spectrum estimation with a bow-tie filter geometry. An advantage in our approach is to use the reconstructed CT images. Because only the CT image is employed as an input, the proposed method is simple and does not require information on the CT geometry. Not all works require a special phantom (Zhao, Niu, et al. 2014) like us, however, it requires to derive the projection data, which is not always available in clinical CT devices. The robustness of our approach was validated using the CT images reconstructed from the system with a different geometry and those with different locations of the Gammex phantom.

2. Methods and Materials

The workflow of this study is shown in Fig. 1, where we first generate datasets composed of an X-ray spectrum and the corresponding virtual CT image of Gammex phantom, with a specific X-ray spectrum generated by a spectral model using `spektr` v.3.0. There, sinograms were produced using a material-based forward projection algorithm (MBFPA), and sequential image reconstruction using filtered back projection (FBP) was performed with the produced sinograms. The details are given in Section 2.2. The generated datasets are then used to develop the spectrum estimation models based on the ANN as seen in Section 2.3. In this study, the spectrum models were differently developed with and without a bow-tie filter. The modeling process with the bow-tie filter is provided in Section 2.4. The verification in these models is shown in Section 2.4 as well as Result section. The feasibility of our model in the real CT device is also provided with the sinogram acquired in Activion16 (Canon Medical System, Japan) as shown in Section 2.6.

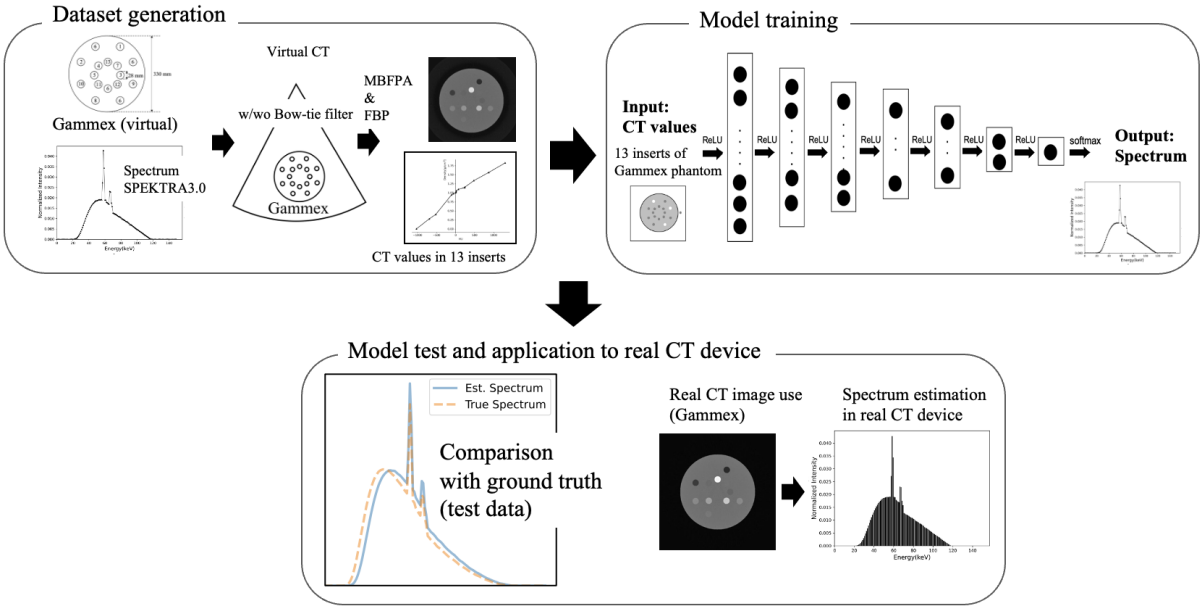

Figure 1. Workflow for the X-ray spectrum estimation.

2.1. Virtual CT system

In the proposed method, a sinogram was first produced by MBFPA based on the information of both the materials in an object and the X-ray spectrum. MBFPA calculates the intensity ratio of X-rays at the ith detector, I_i, to the source, I_0, according to Lambert-Beer's law with the line attenuation coefficient $\mu(E)$,

$$\frac{I_i}{I_0} = \frac{\sum_E \alpha(E) n_0(E) e^{\sum_j -a_{ij}\mu_j(E)}}{\sum_E \alpha(E) n_0(E)}, \tag{1}$$

where E denotes the photon energy (discretized with a bin width of 1 keV in this study). $\alpha(E)$ is the fraction of the corresponding photon energy bin, n_0 is the photon number in the X-ray source, and a_{ij} is the photon pass length in voxel j of the object, representing an element known as "system matrix". The attenuation in the jth voxel, $\mu_j(E)$, can be expressed as the sum of the attenuation coefficients for each element m with atomic number Z_m:

$$\mu_j(E) = \sum_m w_m \mu_j(E, Z_m), \tag{2}$$

where w_m denotes the weight (fraction) of the mth element in that voxel. For the energy range (80–140 keV) and the elements included in the object (Gammex phantom) considered in this study, the attenuation coefficient $\mu_j(E, Z_m)$ can be described as the sum of the processes of the photoelectric effect and Compton scattering:

$$\mu_j(E, Z_m) = \rho Z_m \frac{N_A}{A_m} \left[\sigma_{\mathrm{PE}}(E, Z_m) + \sigma_{\mathrm{Comp}}(E)\right], \tag{3}$$

where ρ, N_A, and A_m denote physical density, the Avogadro constant, and atomic weight, respectively. σ_{PE} and σ_{Comp} are the photoelectric and Compton cross sections, respectively, where we employed an empirical formula fitted with the energy and atomic number for σ_{PE} (Hirschfelder, Adams, et al. 1948; Yao and Leszczynski 2009), and the theoretical formula for σ_{Comp} (Klein and Nishina 1928; Yao and Leszczynski 2009). Consequently, virtual projections can be simulated in a ray-tracing manner to efficiently generate sinograms.

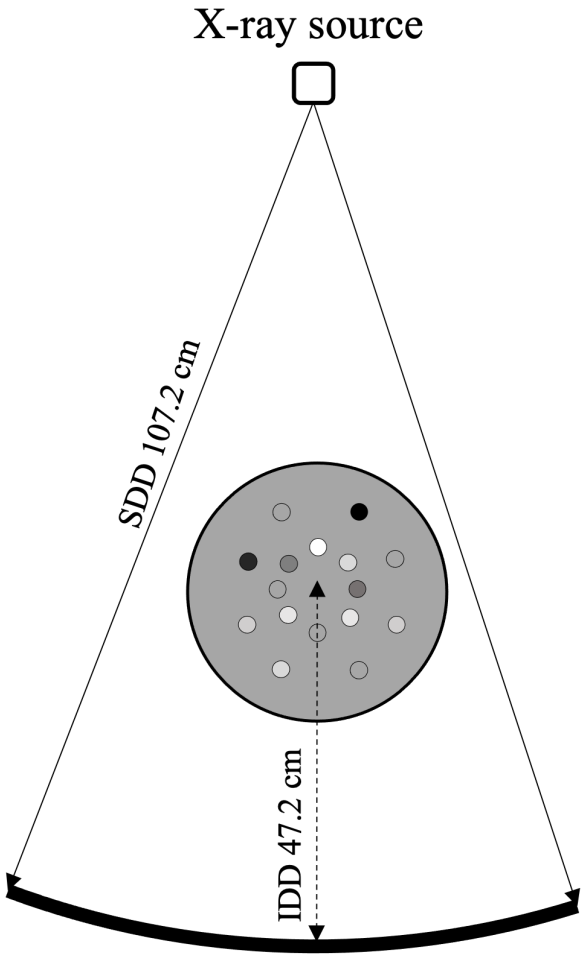

Figure 2. Geometry of the simulated CT system. IDD: isocenter-to-detector distance; SDD: source-to-detector distance. In this study, an SDD of 107.2 cm and IDD of 47.2 cm were used. In total, 798 detector elements were used, and the width of each detector element was 0.103 cm.

The geometry of the simulated CT with relevant factors is shown in Fig. 2, where Activion16 (Canon Medical Systems, Japan) was modeled. The source and detectors were rotated by 360° in 0.45° increments (in total 800 projections). A total of 798 detectors were aligned at equal intervals (0.103 cm).

A noise is present in actual CT acquisition. In this study, the noise on X-ray detectors was modeled with Gaussian distributed random noise to the X-ray intensity

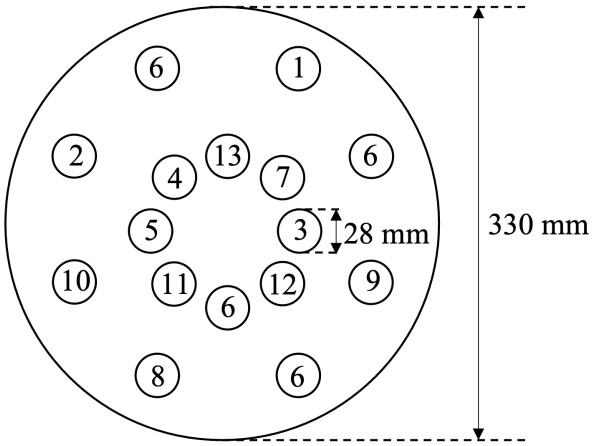

Figure 3. Axial image in virtual Gammex phantom (Model 467). The number in each insert corresponds to that in Table I.

as,

$$I_i^* = I_i + \sigma_i z_i, \tag{4}$$

where I_i^* is the X-ray intensity generated in the ith detector of a virtual CT, and z_i is a standard normal random variable. Although the Poisson distribution is usually used in the noise model, it can be approximated by the Gaussian distribution with the standard deviation $\sigma_i \sim I_0\sqrt{I_i}$ in the situation that the intensity is enough high. Especially, we set $10^5 \leq I_0 \leq 10^6$ to have the same order of signal-to-noise (SNR) ratio as that observed in a real CT system (SNR $\sim$ 10, see section 2.6).

Using the sinograms generated by a fully simulation-based algorithm, CT images with a size of 512×512 mm^2 and a 1-mm pixel scale were reconstructed by FBP with the Shepp-Logan filter. Although this geometry was fixed in the virtual CT image production for the training data, we generated additional CT images with different geometries mimicking tomotherapy (Ruchala et al. 1999), as described in Section 2.5. The next subsection presents the details of the X-ray spectra and the digital Gammex phantom used to generate CT images utilizing the above virtual CT system.

2.2. Data generation

In spectrum generation, we used `spektr` v.3.0, which is a computational tool for X-ray spectrum modeling of a specific tube voltage by fitting the MC simulation with various situations (Punnoose et al. 2016). In this study, 10,000 spectra were generated by randomly sampling the tube voltage in the range of 80–140 kVp, ripple in the range of 0%–100%, Al-filtration thickness in the range of 0.5–10 mm, and Cu-filtration thickness in the range of 0–0.5 mm, with a bin width of 1 keV. Each generated spectrum was normalized such that the spectrum could be regarded as the probability distribution of the photon energy. With the aforementioned virtual CT system, 10,000 CT images corresponding to 10,000 energy spectra sampled from the spectrum model

Table 1. Tissue substitutes in the Gammex phantom (Gomà, Almeida, and Verhaegen 2018), where the physical density was obtained from the data provided by the manufacturer.

Name	Physical density	H	C	N	O	Mg	P	Ca
1.LN-300 Lung	0.30	0.025	0.178	0.006	0.054	0.034	0	0
2.LN-450 Lung	0.48	0.041	0.286	0.009	0.087	0.054	0	0
3.AP6 Adipose	0.949	0.086	0.686	0.021	0.154	0	0	0
4.BR-12 Breast	0.984	0.085	0.690	0.023	0.176	0	0	0.009
5.Water Insert	1.000	0.112	0	0	0.888	0	0	0
6.CT Solid Water	1.016	0.081	0.683	0.024	0.202	0	0	0.023
7.BRN-SR2 Brain	1.051	0.114	0.762	0.018	0.156	0	0	0
8.LV1 Liver	1.090	0.088	0.730	0.023	0.218	0	0	0.025
9.IB Inner Bone	1.138	0.076	0.633	0.022	0.268	0	0.037	0.101
10.B200 Bone Mineral	1.146	0.076	0.636	0.023	0.271	0	0.037	0.102
11.CB2-30% $CaCO_3$	1.333	0.089	0.713	0.028	0.341	0	0	0.160
12.CB2-50% $CaCO_3$	1.560	0.074	0.649	0.024	0.499	0	0	0.312
13.SB3 Cortical Bone	1.822	0.062	0.572	0.034	0.665	0	0	0.488

were generated. In particular, 7,000 were used in the training of the spectrum estimation model, and 1,500 were used in the model validation. The rest were used in the model test, which evaluated the model accuracy without overestimation owing to overfitting.

We chose the Gammex phantom (Gammex Inc., Middleton, WI) for the object to be used in spectrum estimation. The Gammex phantom is most frequently used for CT-to-density calibration in the treatment planning of radiotherapy because its tissue substitutes can be a good representative of biological tissues within the energy range relevant to CT. The widespread use of phantoms, such as the Gammex phantom, is advantageous in the clinical application of spectrum estimation. We developed a digital Gammex phantom as shown in Fig. 3, where the size was set to 512×512 mm^2, with a pixel scale of 1 mm. Table 1 indicates the material weights in each insert, in which $m \in$ H, C, N, O, Mg, P, and Ca were considered in Eq. (1) (Gomà, Almeida, and Verhaegen 2018).

2.3. Spectrum estimation based on ANN

As shown in Fig.4, the ANN was designed to estimate the X-ray spectrum from the CT-to-density data of Gammex phantom. The input is a 13-dimensional vector, of which the components are derived from the CT values of the 12 inserts (Fig. 3), except for the water rod (because the CT value for water was set to vanish) and the air outside the phantom. An averaged value over 80 pixels, $\bar{CT}$, was standardized as

$$Z_k = \frac{\bar{CT}_k - \mu_k}{\sigma_k}, \tag{5}$$

in each insert k. Here, μ_k and σ_k are the mean and standard deviation of the training CT data (7,000 Gammex phantom images) for the kth insert. Note that

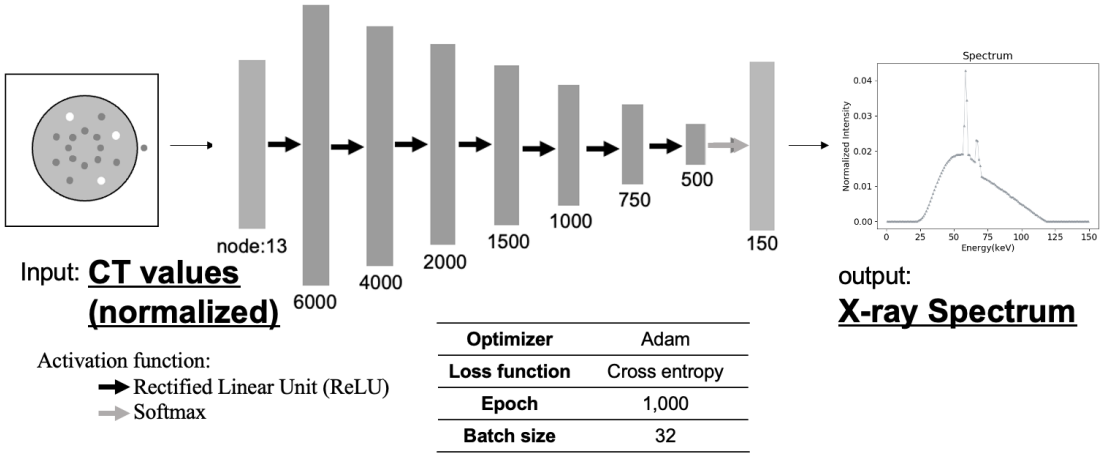

Figure 4. Artificial neural network model to estimate X-ray spectrum from CT-to-density lookup table.

the same μ_k and σ_k are also adapted for application to the validation and test data. The ANN model we developed consists of seven fully connected layers, including 6000,4000,2000,1500,1000,750, and 500 nodes, 7 activation layers, and 7 dropout layers. The activation function used in all activation layers was the rectified linear unit (ReLU), except for the last activation, where the softmax function was employed to output the probability of the photon in each energy bin in the range [1 keV, 150 keV]. The parameters of the ANN model were optimized by employing a cross-entropy error function as a loss function. The convergence of the parameter optimization was verified by monitoring the behavior of the loss function for both the training and validation data. The number of epochs was set to 1,000 whereas the batch size was set to 32, with a learning rate of 0.00001 in the Adam optimizer. Google's deep learning framework TensorFlow (Abadi et al. 2016) (version 1.12.0), and the Keras library (version 2.1.6) were used in this optimization.

2.4. Bow-tie filter model

A bow-tie filter can be used to make the radiation signal uniform within the dynamic range of the detector and to reduce unnecessary radiation dose to the peripheries of a patient. Because the X-ray spectrum varies with its inherent direction depending on the thickness of the bow-tie filter, a simulation, including a bow-tie filter, is essential to model modern CT devices. In this study, we prepared CT spectrum datasets for the system, including a bow-tie filter.

The modeled bow-tie filter was developed as follows. First, the air profile was acquired by setting a 120 kVp without objects (i.e., air scanning) using Activion16. Second, the line attenuation coefficient was evaluated in each source-to-detector direction by assuming a representative of 120 kVp spectrum sampled from spektr (10-mm Al filter, no Cu filter, and 10% ripple). Third, the relative thickness of each

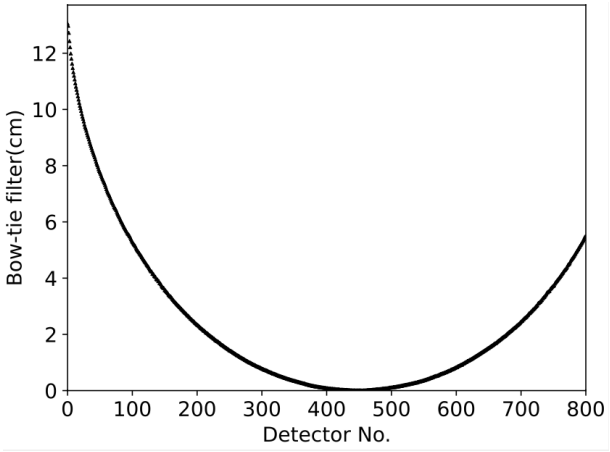

Figure 5. Bow-tie filter thickness (vertical axis) assumed in each detector (horizontal axis), where Al is assumed to be a single composite in the bow-tie filter.

direction in the vertical (0-degree's) direction was evaluated by assuming an appropriate material composed of the bow-tie filter (in this study, we assumed a single component of aluminum), thus the shape can be reconstructed. The bow-tie profile of the virtual CT system reconstructed using this approach is shown in Fig. 5. For data generation, the virtual CT system, spectra, and object models were the same as those described in previous sections. In particular, 10,000 CT images of the Gammex phantom (1,500 for validation and 1,500 for test) were generated with virtual projection using MBFPA, where the bow-tie filtered X-ray spectrum was assumed. The ANN model with the bow-tie filter was trained using the generated CT images labeled by the X-ray spectra before passing through the bow-tie filter.

The above bow-tie filter model is just that in a virtual CT system. In the X-ray spectrum estimation for a real CT system, the training data should be generated with a real bow-tie material/shape. However, it is difficult to model a bow-tie filter in an actual CT system, because the details are usually not opened by vendors. Therefore, in addition to the above bow-tie filter model, which is reconstructed with a certain X-ray spectrum and its air profile at the detector, we performed a simultaneous estimation of both the bow-tie profile and the X-ray spectrum for the real Activion16 machine; the shape of the bow-tie filter was iteratively optimized through the X-ray spectrum estimation, as shown in Fig. 6. In the actual optimization, we assumed aluminum as a composite material of the bow-tie filter, and the X-rays in each source-to-detector direction were attenuated depending on the Al thickness. The convergence was judged with the difference between the estimated spectrum and that in the previous step.

2.5. Verification

To evaluate the estimation accuracy of the developed ANN model, 1,500 CT images, which were not included in the model development, were used as inputs. Subsequently, the output spectra were generated by the models with and without a bow-tie filter.

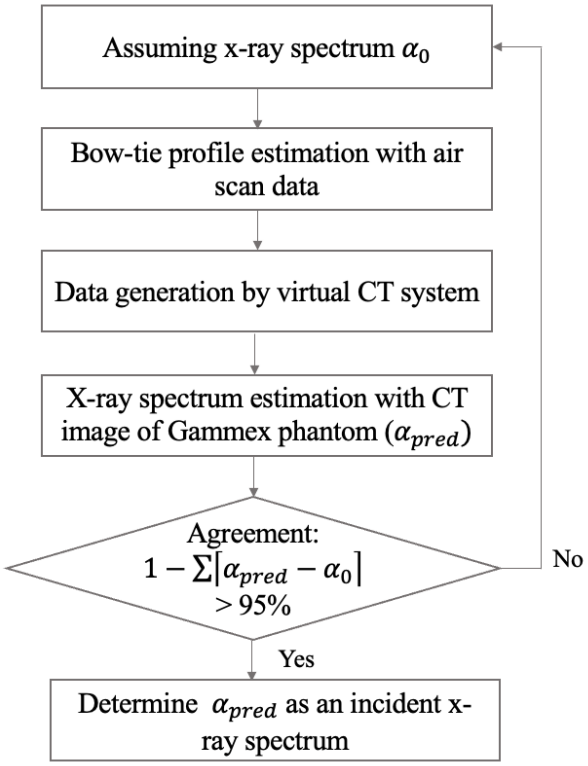

Figure 6. Flowchart to determine an incident X-ray spectrum in real CT device involving bow-tie filter, where we determined that the spectrum assumed in the bow-tie profile estimation agrees with that estimated by the ANN model with a real CT image for the Gammex phantom. The agreement defined in Eq. (6) more than 95% was judged to be converged in this study.

The model accuracy was measured by the root mean squared error (RMSE) and the difference in mean X-ray energy. In addition we employed the agreement defined as "one minus the absolute error", which provides 1 in the complete overlapping and -1 in the no overlapping with the ground truth,

$$\text{Agreement} \equiv \ 1 - \sum_{i}^{N_{bin}} |\alpha_{pred}(E_i) - \alpha_{true}(E_i)|, \tag{6}$$

where $N_{bin} = 150$ and $i \in 1, 2, \cdots, 150$. $\alpha_{pred}(E_i)$ is the predicted spectrum fraction in the ith bin, and $\alpha_{true}(E_i)$ is the spectrum fraction in the ground truth. To verify the robustness of the model, test images prepared using different CT geometries were employed. Consequently, we used the geometry in tomotherapy with SDD = 142.6 cm and IDD = 57.6 cm, which is considerably different from the conventional CT device. In addition, the influence of the phantom location was evaluated by a 1-cm offset for the phantom of the test data in the upper direction. In both tests, 1,500 (CT) images were obtained.

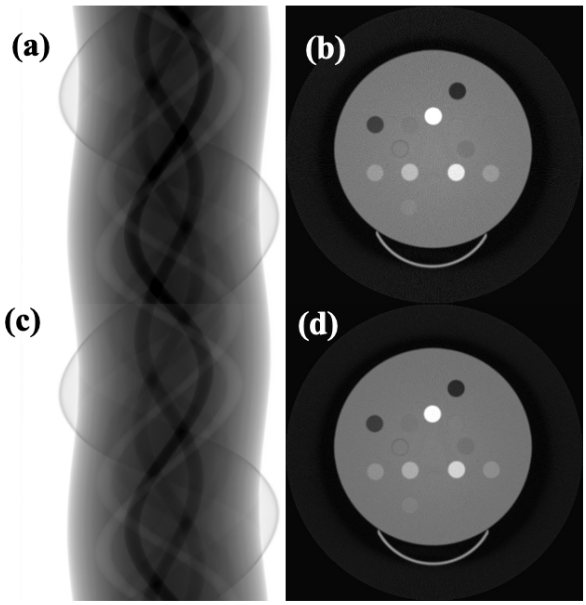

Figure 7. Sinogram acquired in Activion16 ((a) 100 kVp and (c) 120 kVp) and the corresponding CT image ((b) 100 kVp and (d) 120 kVp).

2.6. Experimental data

The developed model considering a bow-tie filter was applied in a real CT system, Activion16. The real Gammex phantom Model467 with the physical density shown in Table 1 was scanned with nominal tube voltages of 100 kVp and 120 kVp at tube current of 100 mA, with an acquisition time of 1.5 s. With these conditions, the SNR of the basis material in the Gammex phantom (solid water) was 11.2 and 20.9, for 100 kVp and 120 kVp, respectively. As described in Section 2.4, an initial bow-tie profile was created using the assumed X-ray spectrum and air scanning. Thereafter, the X-ray spectrum was estimated by an ANN trained with this bow-tie profile. The estimated X-ray spectrum was again used to create the bow-tie profile, and the simulation was performed until convergence was achieved. Although the real CT system is equipped with the reconstruction software itself, we used the same CT reconstruction code as used in the virtual CT system to avoid additional differences other than the system geometry, such as pre-processing (e.g., angle interval in the sinogram), reconstruction filter, and post-processing (e.g., beam-hardening correction) between the CT images used in the training and testing. Figure 7 shows the sinogram and the corresponding CT image for the Gammex phantom in 100 kVp and 120 kVp operations.

2.7. Estimation using virtual step wedge and maximum likelihood expectation maximum method

In this study, the X-ray spectrum estimation using the maximum likelihood expectation maximum (MLEM) method was also developed by using the "virtual step wedge". This

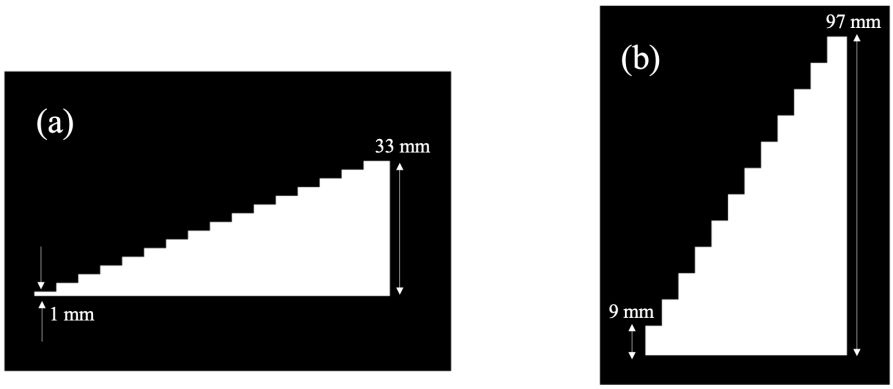

Figure 8. Virtual step wedge.

method has already been applied with the real step wedge and the clinical CT machine (Sidky et al. 2005; Duan et al. 2011). This study applies it to see the feasibility of the proposed virtual system for the different estimation model.

Figure 8 shows the virtual step wedge phantoms developed here, where (a) has 16 steps with aluminium (Al, 2.7 g/cm^3) composition, and (b) has 12 steps with polycarbonate ($C_{16}H_{14}O_3$, 1.21 g/cm^3) composition, and the projection data of these objects were generated by virtual CT system of Fig. 2. Based on the MLEM approach, the spectrum fraction of k-th energy bin in $t+1$-th iteration, $\alpha_k^{(t+1)}$ can be renewal with the spectrum fraction $\alpha_k^{(t)}$ in t-th iteration as,

$$\alpha_k^{(t+1)} = \frac{\alpha_k^{(t)}}{\sum_l X_{lk}} \sum_l \frac{X_{lk} n_l}{\sum_{k'} X_{lk'} \alpha_{k'}^{(t)}}, \tag{7}$$

where $X_{lk} = n_{0,l} \exp\left(-\sum_j a_{ij} \mu_j(E_k)\right)$ and $n_{0,l}$ and n_l are the photon count at source and at l-th detector, respectively.

Using spektr, 20 projections (for aluminium and polycarbonate phantoms) corresponding to 10 energy spectra sampled from the spectrum model, where the energy spectra from 120 kVp was employed, were generated by the way described in 2.1. Also, same intensity of the noise as described in 2.2 was added. In addition, a specific energy spectrum of 120 kVp with the Al filter of 1-mm thickness was derived and was used as the initial input $\alpha_i^{(0)}$. Then the spectrum was estimated from both projections of aluminium and polycarbonate phantoms. The MLEM result of these 10 data was evaluated by the agreement as well as RMSE to the ground truth (generated by spektr). To see the dependency of the initial input, the result which an energy spectrum of 80 kVp was used as the initial input was also evaluated.

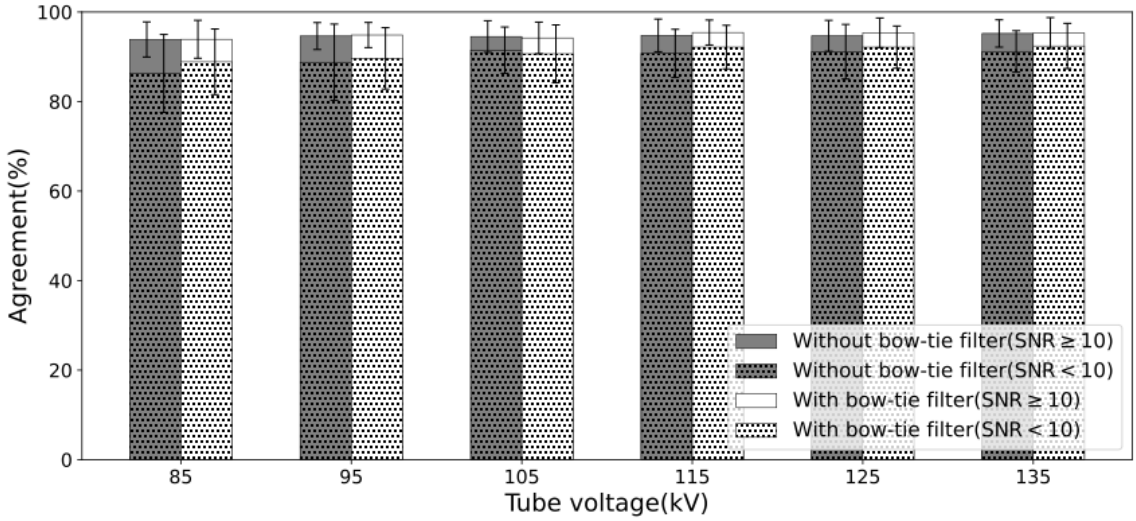

Figure 9. Averaged agreement defined in Eq. (6) in a tube voltage range of 10-kVp bin; (dark gray bar) without the bow-tie filter model, and (white bar) with the bow-tie filter model. Dotted bars indicate the result, including all test data, whereas normal bars indicate the result only, including the test data presenting the CT image with an SNR of ≥ 10 in Gammex basis material (solid water). The error bar indicates the standard deviation.

3. Results

3.1. Estimated X-ray spectrum without/with bow-tie filter

Figure 9 shows the result of the agreement measure defined in Eq. (6) for test data, where the average with a standard deviation in each tube voltage range with 10-kVp interval are compared. The dotted bars indicate the results, including all test data, whereas the normal bars indicate the result only, including the test data presenting the CT image with an SNR of ≥ 10 in Gammex basis material (solid water). This result indicates that most of the test data can be estimated with an agreement of $\geq 80\%$. The estimation accuracy was better in CT images acquired at high tube voltages. Owing to this tendency, the ANN model with bow-tie filter (dotted white bars) slightly improves the agreement without a bow-tie filter (dotted dark-gray bars), because the presence of the bow-tie filter makes the X-ray hard. This figure also shows the impact of noise on CT images, and the evaluated agreements with less noise on CT images (normal bars) are high compared to those with all test data (dotted bars), implying that the spectrum estimation is expected to be successfully performed if the CT image is acquired with the condition considering SNR ≥ 10 on a Gammex basis.

Figure 10 shows spectra estimated in the test data for SNR ≥ 10 without a bow-tie filter for different ranges of tube voltages: 80–100 kVp, 100–120 kVp, and 120–140 kVp in the top row, middle row, and bottom row, respectively. The first, second, and third columns show the spectra for the best estimation, median estimation, and worst estimation in agreement measure, respectively. The figure shows that the estimation is

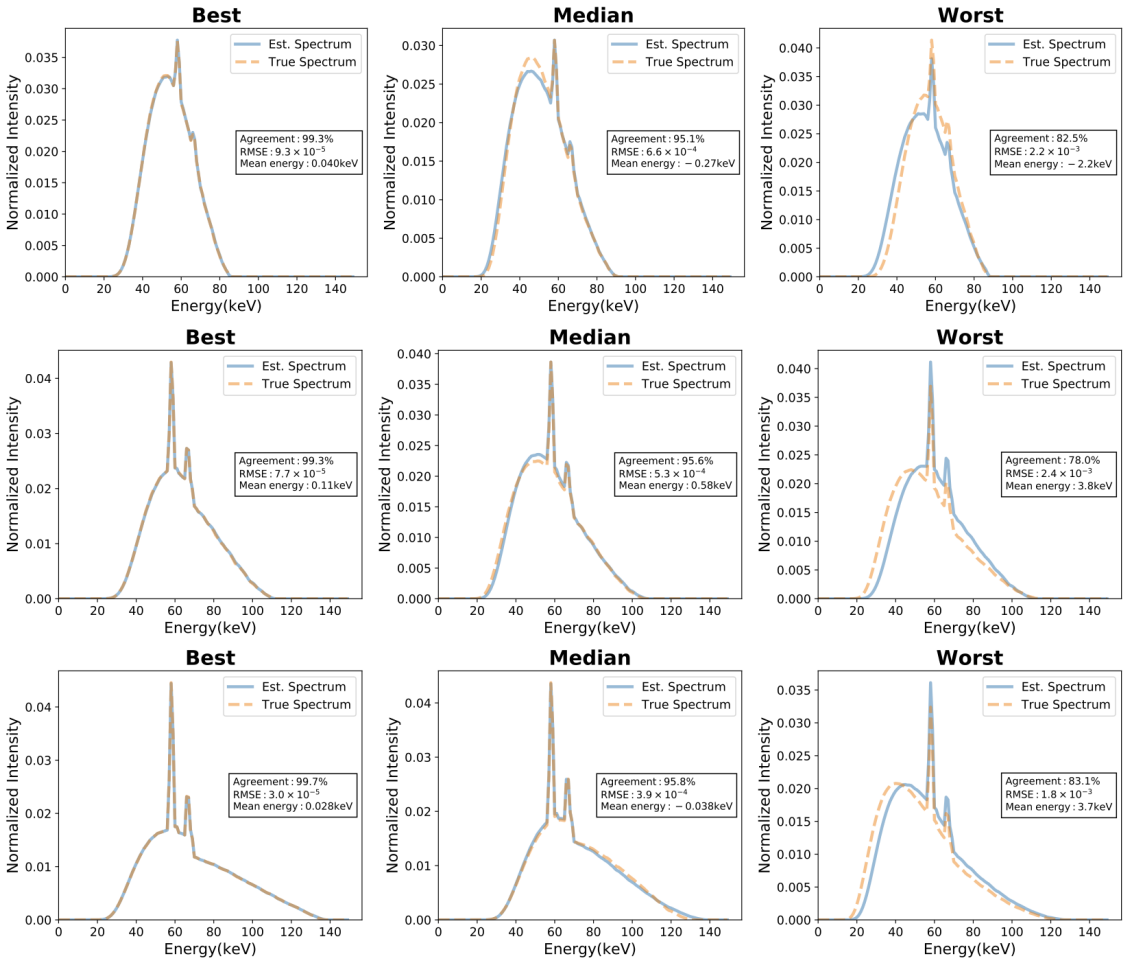

Figure 10. Estimated X-ray spectra without bow-tie filter ; (top row) 80–100 kVp, (middle row) 100–120 kVp, and (bottom row) 120–140 kVp. The first, second, and third columns show the spectra for the best estimation, median estimation, and worst estimation in agreement measure defined in Eq.(6).

still well for median in the rank of estimated accuracy (second row). Some deviation can be observed for the worst result (third row), although the agreement is more than 80% for almost all data. This tendency is similar to that of the bow-tie filter model, as depicted in Fig. 11, where the median result is good, whereas the worst results exhibit some differences. The result showing an agreement of less than 80% was only one case for both the without/with bow-tie filter models. Although there are some failures in the estimation, the overall estimation accuracy would be sufficiently high without CT image degradation.

3.2. Influence of the different geometry in test data

In Fig. 12, the results of the test CT data acquired in different geometries from those used in the training data are indicated, where (a) different source-to-isocenter as well as different source-to-detector distances are employed and (b) the displacement of the

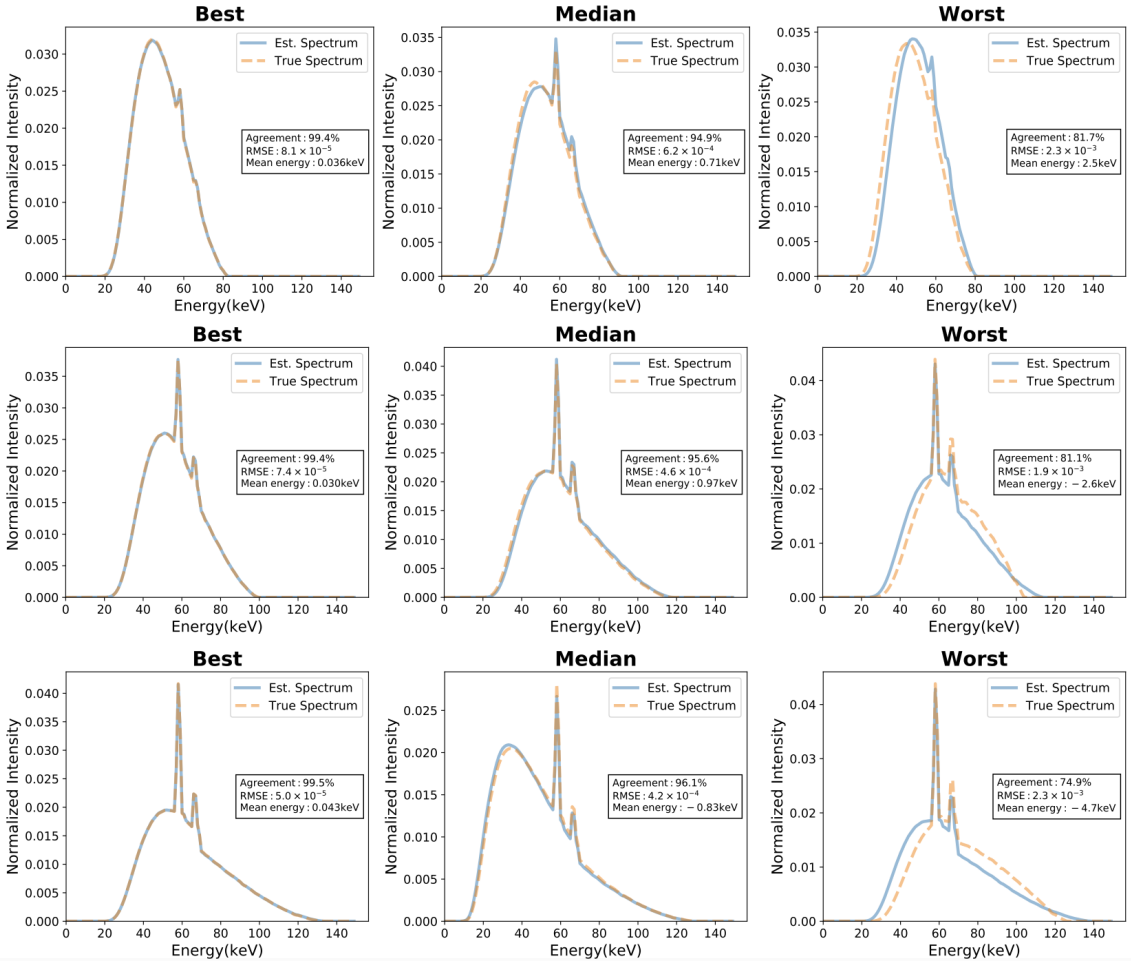

Figure 11. Estimated X-ray spectra with bow-tie filter; same as in Fig. 10.

phantom location (1-cm shift) is applied. Here, the blue bars indicate the RMSE using the identical geometry model between the training and test data, whereas the red bars indicate the RMSE using the different geometry models between them. A model without a bow-tie filter was employed in both cases. As we can observe, the difference between the blue and red is significantly small even in the existing apparent discrepancy in the geometry of CT scanning, although the paired t test indicated that the geometrical variation between the training and testing datasets significantly affects the estimation accuracy, except for the low tube voltage . Because the statistical difference was evaluated with a large amount of test data (nearly 500 test data in each comparison), then the pygmy difference could be detected owing to this data size. The present test for the robustness of CT geometry was performed with the worst case in CT scanning, and the CT geometry in ordinal CT devices is not different from Activion16 in comparison with that in tomotherapy, which requires a large bore size for radiation therapy. The registration of phantom location can be easily performed within 1 cm even in a manual setting. Thus, the present results suggest that our approach can estimate the X-ray spectrum without accurate knowledge of the system geometry.

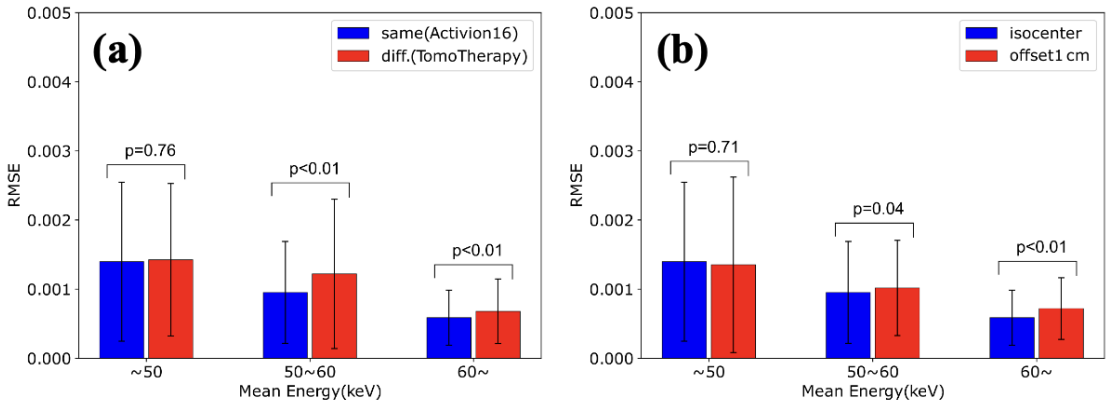

Figure 12. Comparison between identical geometry (blue) and different geometry (red) used in the preparation of test data; (a) different source-to-isocenter as well as the different source-to-detector distances is employed, and (b) displacement of the phantom location (1-cm shift) is applied. The *p*value was calculated using the paired *t* test.

3.3. Estimated X-ray spectrum in real CT device

Figures 13(a) and (b) show the estimated X-ray spectrum in real Activion16 CT device by following the process of Fig. 6. The estimated spectra in 3*rd*-step (solid curves) are indicated as well as the initial ones (dotted curves). The agreements between the reconstructed spectra in the 2*nd*-step and those in the 3*rd*-step were 96.0% for 100 kVp and 98.7% for 120 kVp, respectively, and therefore the spectra were judged to be converged in the 3*rd*-step. Because there is no ground truth for the energy spectra in a real CT device, we cannot provide the actual accuracy of this estimation; however, we can only conclude that the predicted X-ray spectrum has a reasonable form; a similar spectrum may be reproducible by the spectrum model. In the real CT images used here, the SNRs for the basis of the Gammex phantom were 11.2 and 20.9, for 100 kVp and 120 kVp, respectively, thus the prediction is expected to be successful, as shown in Fig. 11. The simultaneously determined profile of the bow-tie filter, assuming the Al material, is depicted in Fig. 13(c), which shows that convergence is rapidly achieved with a reasonable initial 120 kVp spectrum sampled from spektr (10-mm Al filter, no Cu filter, and 10% ripple).

3.4. Estimated X-ray spectrum using virtual step wedge and MLEM method

Figure 14(a) shows the representative estimated spectrum using virtual step wedge and MLEM method with an initial energy spectrum derived from spektra in 120 kVp and 1-mm thickness Al filter, as described in 2.7. The results of 10-averaged agreement and RMSE are inserted in the figure, where the agreement (95.1%) and the RMSE (5.2×10^{-4}) are comparable with those using the Gammex phantom and the ANN model. This result implies that our proposed method, without the specific phantom such as the step wedge, can be estimated equivalently to the previously proposed method.

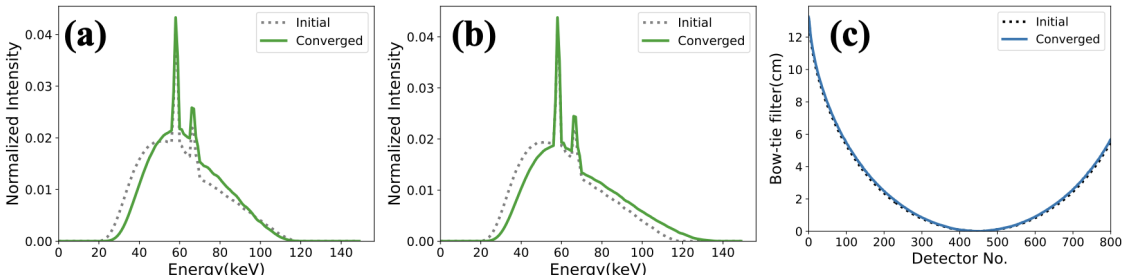

Figure 13. Estimated X-ray spectrum in real Activion16 CT device; (a) 100 kVp and (b) 120 kVp. The corresponding Al-equivalent bow-tie profile is shown in (c). "Initial" indicates the initial spectra and the bow-tie profile reproduced with an air sinogram by assuming 120 kVp spectrum sampled from spektr (10-mm Al filter, no Cu filter, and 10% ripple (see 2.4), whereas "Converged" indicates the converged those, where the agreement more than 95% with the previous step (the current case: $3rd$-step) was judged to be converged.

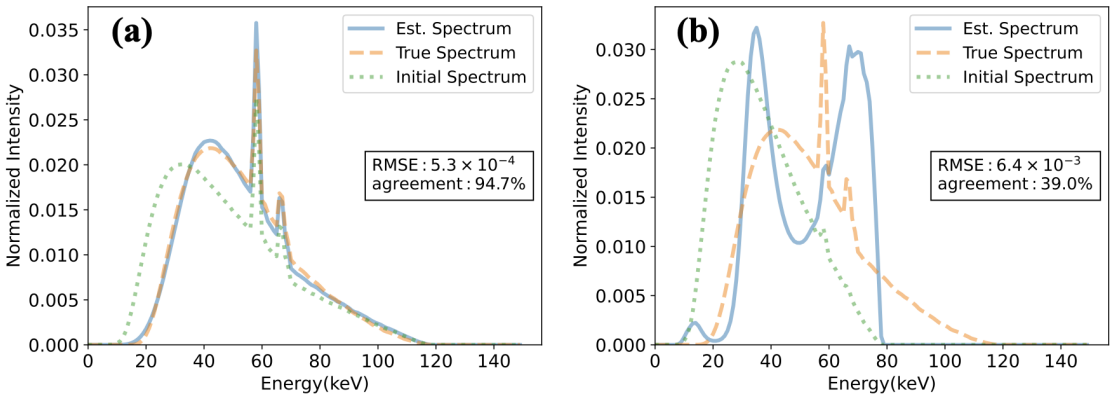

Figure 14. Estimated X-ray spectrum with virtual step wedge and maximum likelihood expectation maximum (MLEM) method; (a) initial energy spectrum with 120 kVp and 1-mm thickness Al filter (b) initial energy spectrum with 80 kVp and 1-mm thickness Al filter. The proper initial input is important to estimate the energy spectrum in this method.

Figure 14(b) shows the estimated result with the energy spectrum from the spektra for 80 kVp and 1-mm thickness Al filter as the initial input. In the estimation using the MLEM approach, the initial value can influence the accuracy, and therefore, one should select the reasonable spectrum from the prior knowledge such as the tube voltage to be estimated.

4. Discussion

In the present study, we newly proposed a simulation-based method for model creation, in which CT datasets labeled with the corresponding X-ray spectrum were generated by the virtual CT system, and the estimation model was trained with these datasets. With our method, spectrum estimation can be easily performed by scanning Gammex

phantom in a real CT system without a special setup. By comparing with the previously proposed approach using virtual step wedge and MLEM method in projection domain, we can say that our approach, using Gammex phantom and ANN method in reconstructed domain, is comparable in the accuracy of energy spectrum. The present method allows the use of other phantoms, and more sophisticated phantoms might be expected to increase the estimation accuracy. However, for application purposes, the present approach, including the use of the Gammex phantom, is simpler compared to other proposed methods.

The present results also show that our method can estimate the spectrum satisfactorily even when equipped with a bow-tie filter. In addition, it was confirmed that the estimation result obtained using the real Gammex phantom CT can produce a realistic spectrum. This implies that our method may be reliable for estimating the X-ray spectrum, as well as the bow-tie filter shape. Furthermore, we emphasized that our method only requires the CT image of the Gammex phantom, and does not require special geometrical calibration, except for the normal calibration executed in the CT device setting. On the other hand, the model with bow-tie filter could involve the model without bow-tie filter by including both dataset with/without bow-tie filter. However, the present model did not. This is one of the limitations in our model regarding the generalization, and it remains as the future development.

Our model is expected to be robust in the geometrical variation of CT systems because of the use of CT images as an input, in which the system geometry can be wasted after obtaining the geometry of the CT object. The present study investigated the robustness of the estimated model regarding the discrepancy in the CT geometry acquired between the training data obtained with the Activion16 model and the testing data obtained with the tomotherapy model. The statistical result showed the significant difference between them; however, the amount of the difference was quite small. Because the CT geometry in tomotherapy is considerably different from that in normal CT devices, it can be considered that the present analysis indicates the worst scenario, and the difference in the CT geometry does not affect the X-ray spectrum estimation so much. In addition to the CT geometry, we investigated the influence of the phantom location in the CT acquisition, and the situation was similar to that in the CT geometry; the statistical difference was found in a certain range of the tube voltage; however, the amount was small. Thus, the difference won't affect the result. Consequently, the proposed method is sufficiently robust, and can be generalized in any CT geometry and acquisition. In such cases, phantoms other than the Gammex phantom should be examined.

5. Conclusion

In this study, we developed a new method for estimating the incident X-ray spectrum for diagnostic CT systems based on a virtual CT generation system. The present approach used the information obtained from the reconstructed CT images of the

Gammex phantom to avoid the estimation accuracy not to be affected significantly by the geometry in CT scanning. Our approach allows the inclusion of a model with a bow-tie filter, and a reasonable X-ray spectrum can be reconstructed from experimental data with a simultaneous estimation of the shape of the bow-tie profile. The present work is expected to be applied to the development of a CT reconstruction algorithm, such as material decomposition.

Acknowledgments

This study was supported by JSPS KAKENHI (grant no. 19K08201).

References

Abadi, Martın et al. (2016). "Tensorflow: Large-scale machine learning on heterogeneous distributed systems". In: *arXiv preprint arXiv:1603.04467*.

Armbruster, Benjamin, Russell J Hamilton, and Arthur K Kuehl (2004). "Spectrum reconstruction from dose measurements as a linear inverse problem". In: *Phys. Med. Biol.* 49.22, p. 5087.

Bazalova, Magdalena and Frank Verhaegen (2007). "Monte Carlo simulation of a computed tomography x-ray tube". In: *Phys. Med. Biol.* 52.19, p. 5945.

Bishop, Christopher M and Nasser M Nasrabadi (2006). *Pattern recognition and machine learning*. Vol. 4. 4. Springer.

Boone, John M (2010). "Method for evaluating bow tie filter angle-dependent attenuation in CT: theory and simulation results". In: *Med. Phys.* 37.1, pp. 40–48.

Duan, Xinhui et al. (2011). "CT scanner x-ray spectrum estimation from transmission measurements". In: *Med. Phys.* 38.2, pp. 993–997.

Duisterwinkel, HA et al. (2015). "Spectra of clinical CT scanners using a portable Compton spectrometer". In: *Med. Phys.* 42.4, pp. 1884–1894.

Francois, P, A Catala, and Ch Scouarnec (1993). "Simulation of x-ray spectral reconstruction from transmission data by direct resolution of the numeric system AF= T". In: *Med. Phys.* 20.6, pp. 1695–1703.

Gomà, Carles, Isabel P Almeida, and Frank Verhaegen (2018). "Revisiting the single-energy CT calibration for proton therapy treatment planning: a critical look at the stoichiometric method". In: *Phys. Med. Biol.* 63.23, p. 235011.

Ha, Wooseok et al. (2019). "Estimating the spectrum in computed tomography via Kullback–Leibler divergence constrained optimization". In: *Med. Phys.* 46.1, pp. 81–92.

Hasegawa, Yu et al. (2021). "Estimation of X-ray energy spectrum of cone-beam computed tomography scanner using percentage depth dose measurements and machine learning approach". In: *Journal of the Physical Society of Japan* 90.7, p. 074801.

Hastie, Trevor et al. (2009). *The elements of statistical learning: data mining, inference, and prediction*. Vol. 2. Springer.

Hioki, Kazunari et al. (2014). "Absorbed dose measurements for kV-cone beam computed tomography in image-guided radiation therapy". In: *Phys. Med. Biol.* 59.23, p. 7297.

Hirschfelder, Joseph O, Edward N Adams, et al. (1948). "The Penetration of Gamma-Radiation through Thick Layers II. Plane Geometry, Iron, and Lead". In: *Phys. Rev.* 73.8, p. 863.

Klein, Oskar and Yoshio Nishina (1928). "The scattering of light by free electrons according to Dirac's new relativistic dynamics". In: *Nature* 122.3072, pp. 398–399.

Leinweber, Carsten, Joscha Maier, and Marc Kachelrieß (2017). "X-ray spectrum estimation for accurate attenuation simulation". In: *Med. Phys.* 44.12, pp. 6183–6194.

Lin, Yuan et al. (2014). "An angle-dependent estimation of CT x-ray spectrum from rotational transmission measurements". In: *Med. Phys.* 41.6, p. 062104.

Maeda, Koji, Masao Matsumoto, and Akira Taniguchi (2005). "Compton-scattering measurement of diagnostic x-ray spectrum using high-resolution Schottky CdTe detector". In: *Med. Phys.* 32.6Part1, pp. 1542–1547.

Matscheko, G and G Alm Carlsson (1989). "Compton spectroscopy in the diagnostic x-ray energy range: I. Spectrometer design". In: *Phys. Med. Biol.* 34.2, p. 185.

McKenney, Sarah E et al. (2011). "Experimental validation of a method characterizing bow tie filters in CT scanners using a real-time dose probe". In: *Med. Phys.* 38.3, pp. 1406–1415.

Perkhounkov, Boris et al. (2016). "X-ray spectrum estimation from transmission measurements by an exponential of a polynomial model". In: *Medical Imaging 2016: Physics of Medical Imaging*. Vol. 9783. International Society for Optics and Photonics, 97834W.

Punnoose, Jacob et al. (2016). "spektr 3.0—A computational tool for x-ray spectrum modeling and analysis". In: *Med. Phys.* 43.8Part1, pp. 4711–4717.

Ruchala, KJ et al. (1999). "Megavoltage CT on a tomotherapy system". In: *Phys. Med. Biol.* 44.10, p. 2597.

Ruth, Christopher and Peter M Joseph (1997). "Estimation of a photon energy spectrum for a computed tomography scanner". In: *Med. Phys.* 24.5, pp. 695–702.

Sidky, Emil Y et al. (2005). "A robust method of x-ray source spectrum estimation from transmission measurements: Demonstrated on computer simulated, scatter-free transmission data". In: *Journal of applied physics* 97.12, p. 124701.

Silberstein, Ludwik (1932). "Determination of the spectral composition of X-ray radiation from filtration data". In: *JOSA* 22.5, pp. 265–280.

Spezi, Emiliano et al. (2009). "Monte Carlo simulation of an x-ray volume imaging cone beam CT unit". In: *Med. Phys.* 36.1, pp. 127–136.

Stampanoni, Marco et al. (2001). "Computer algebra for x-ray spectral reconstruction between 6 and 25 MV". In: *Med. Phys.* 28.3, pp. 325–327.

Taleei, R and M Shahriari (2009). "Monte Carlo simulation of X-ray spectra and evaluation of filter effect using MCNP4C and FLUKA code". In: *Applied Radiation and Isotopes* 67.2, pp. 266–271.

Waggener, Robert G et al. (1999). "X-ray spectra estimation using attenuation measurements from 25 kVp to 18 MV". In: *Med. Phys.* 26.7, pp. 1269–1278.

Whiting, Bruce R et al. (2014). "Measurement of bow tie profiles in CT scanners using a real-time dosimeter". In: *Med. Phys.* 41.10, p. 101915.

Yang, Kai et al. (2017). "Direct and fast measurement of CT beam filter profiles with simultaneous geometrical calibration". In: *Med. Phys.* 44.1, pp. 57–70.

Yao, Weiguang and Konrad W Leszczynski (2009). "An analytical approach to estimating the first order x-ray scatter in heterogeneous medium". In: *Med. Phys.* 36.7, pp. 3145–3156.

Zhao, Wei, Kai Niu, et al. (2014). "An indirect transmission measurement-based spectrum estimation method for computed tomography". In: *Phys. Med. Biol.* 60.1, p. 339.

Zhao, Wei, Don Vernekohl, et al. (2018). "A unified material decomposition framework for quantitative dual-and triple-energy CT imaging". In: *Med. Phys.* 45.7, pp. 2964–2977.

Zhao, Wei, Lei Xing, et al. (2017). "Segmentation-free x-ray energy spectrum estimation for computed tomography using dual-energy material decomposition". In: *Journal of Medical Imaging* 4.2, p. 023506.